NJC
New Journal of Chemistry
A journal for new directions in chemistry

Accepted Manuscript

This article can be cited before page numbers have been issued, to do this please use: M. V. Grudova, D. M. Gil, V. N. Khrustalev, E. V. Nikitina, A. A. Sinelshchikova, M. Grigoriev , A. V. Kletskov, A. Frontera and F. I. Zubkov, *New J. Chem.*, 2020, DOI: 10.1039/D0NJ04328A.

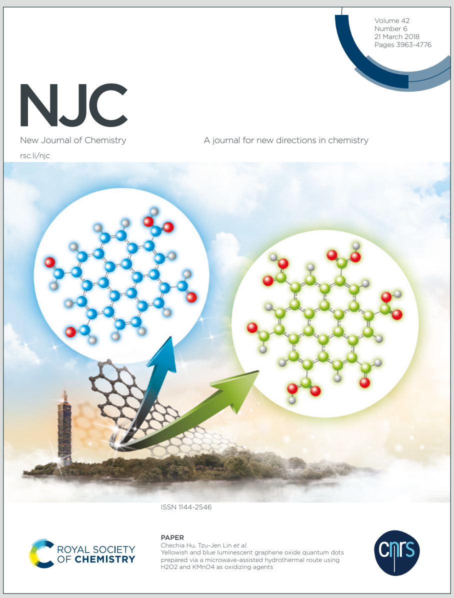

Synthesis, X-ray characterization and theoretical study of 3a,6:7,9a-diepoxybenzo[*de*]isoquinoline derivatives: on the importance of F···O interactions

Mariya V. Grudova,[1] Diego M. Gil,[2] Victor N. Khrustalev,[1,3] Eugeniya V. Nikitina,[1] Anna A. Sinelshchikova,[4] Mikhail S. Grigoriev,[4] Alexey V. Kletskov,[1] Antonio Frontera,*[,5] Fedor I. Zubkov*[,1]

[1] Faculty of Science, Peoples' Friendship University of Russia (RUDN University), 6 Miklukho-Maklaya St., Moscow 117198, Russian Federation. Email: fzubkov@sci.pfu.edu.ru

[2] INBIOFAL (CONICET – UNT). Instituto de Química Orgánica. Facultad de Bioquímica, Química y Farmacia. Universidad Nacional de Tucumán. Ayacucho 471. T4000INI. San Miguel de Tucumán. Argentina.

[3] N. D. Zelinsky Institute of Organic Chemistry of RAS, 47 Leninsky Prospect, 119991 Moscow, Russian Federation.

[4] Frumkin Institute of Physical Chemistry and Electrochemistry, Russian Academy of Sciences, Leninsky pr. 31, bld. 4, Moscow 119071, Russian Federation.

[5] Department of Chemistry, Universitat de les Illes Balears, Crta. de Valldemossa km 7.7, 07122 Palma de Mallorca (Baleares), Spain. Email: toni.frontera@uib.es

Abstract

The synthesis, X-ray characterization and Hirshfeld surface analysis of a series of tetrahydro-diepoxybenzo[*de*]isoquinoline derivatives obtained by the tandem [4+2] cycloaddition between perfluorobut-2-yne dienophile ($F_3C–C≡C–CF_3$) and a row of *N*,*N*-bis(furan-2-ylmethyl)-4-R-benzenesulfonamides (*bis*-dienes, R = Me, F, Cl, Br, I) are reported in this manuscript. The implementation of kinetic/thermodynamic control allowed to obtain both "pincer"- and "domino"-types adducts in good/moderate yields. In the solid state, most of the pincer adducts form self-assembled dimers (R = Me, Cl, Br, I) and, contrariwise, the domino adducts form 1D supramolecular chains, which are described in detail herein. Remarkably, in the self-assembled dimers, bifurcated halogen bonds involving one fluorine atom of the CF_3 group and both *O*-atoms of sulfonamide are formed, which have been analyzed using DFT calculations, QTAIM and NCIplot computational tools.

View Article Online
DOI: 10.1039/D0NJ04328A

Introduction

Thermodynamic and kinetic control, possible in the course of a wide range of chemical and biochemical transformations, is one of the most powerful tools in the arsenal of modern chemistry.[1–5] The implementation of kinetic or thermodynamic control for synthetic purposes is achievable for the reactions proceeding through multiple possible transition states of varying activation energies and is most often used in the field of pericyclic reactions, in particular in various intra and intermolecular [4+2] cycloaddition reactions. Within the synthetic part of this work a degree of kinetic/thermodynamic control in the course of Diels-Alder reaction of perfluorobutin-2 and *N*,*N*-bis(furan-2-ylmethyl)-4-R-benzenesulfonamides was studied. It is worth mentioning that up to date there is a limited range of examples illustrating this principle to a full extent, and in the majority of such type of transformation cases, no full kinetic or thermodynamic control is achieved (see the reviews mentioned above). Consequently, the formation of mixtures of stereo-, regio-, or chemoisomers under both high and low temperatures is observed. This work continues a series of our studies[6,7] aimed at the establishment of the patterns for tandem [4+2]/[4+2] cycloaddition reactions observed in the course of an interaction between *bis*-dienes and activated alkynes under various conditions.

Taking into account that in this work perfluorobutin-2 was used as an alkyne, it was reasonable to expect the formation of multiple inter- and intramolecular H···Hal and Hal···Hal contacts in the target products. Halogen bonding interactions involving fluorine are attracting the attention of chemists working on supramolecular chemistry and crystal engineering.[8] For instance, it has been evidenced experimentally that the polarization of the electron density on the fluorine atom of the trifluoromethyl group in crystal structures results in the formation of an electron deficient region that facilitates $F^{\delta+}\cdots F^{\delta-}$ halogen bond formation with a non-negligible electrostatic contribution.[9] Chopra's group have also described unusual intramolecular C-F···O=C parallel dipole-dipole alignment that "locks" the molecular conformation of cryocrystallized liquids towards the planarity in fluorinated benzoyl chlorides.[10] Moreover, the importance of $C(sp^2)/(sp^3)$-F···F-$C(sp^2)/(sp^3)$ interactions in organic solids has been studied by QTAIM analysis and demonstrated that they are closed shell in nature and provide local stabilization.[11] More recently, the first two examples of halogen bonding in the $C(sp^3)$–F···$O(sp^3)$ interaction involving a σ hole donating fluorine have been both experimentally and theoretically evidenced.[12] Thus, taking into consideration the high theoretical and practical interest towards halogen bonding as well as the high perspectives of the obtained compounds for corresponding studies, the detailed study of the solid state of the synthesized adduct was assumed to be the second goal of our research.

Herein we report the synthesis and X-ray characterization of a series of tetrahydro-diepoxybenzo[*de*]isoquinoline derivatives (Scheme 1) obtained by tandem [4+2] cycloaddition reactions. The perfluorobut-2-yne (F_3C–C≡C–CF_3) has been used as dienophile and five *N*,*N*-bis(furan-2-ylmethyl)-

4-R-benzenesulfonamides (R = Me, F, Cl, Br, I) as *bis*-dienes. The X-ray structures of all kinetic "pincer" adducts and four thermodynamic "domino" adducts have been obtained. In the solid state, the pincer adducts **7a−10a** form self-assembled dimers whilst the domino adducts form 1D supramolecular chains. In the self-assembled dimers, in addition to multiple C–H···O H-bonding interactions, the F-atoms participate in bifurcated halogen bonding interactions with both O-atoms of sulfonamide that further contribute to the formation of these dimers. By means of MEP surface analysis we demonstrate that the distribution of electron density is anisotropic at the F-atom that participates in such interaction (it is polarized) and consequently suitable for receiving the charge from the electron rich *O*-atoms. The existence and an attractive nature of the F···O contacts is further supported by QTAIM and NCIplot analyses.

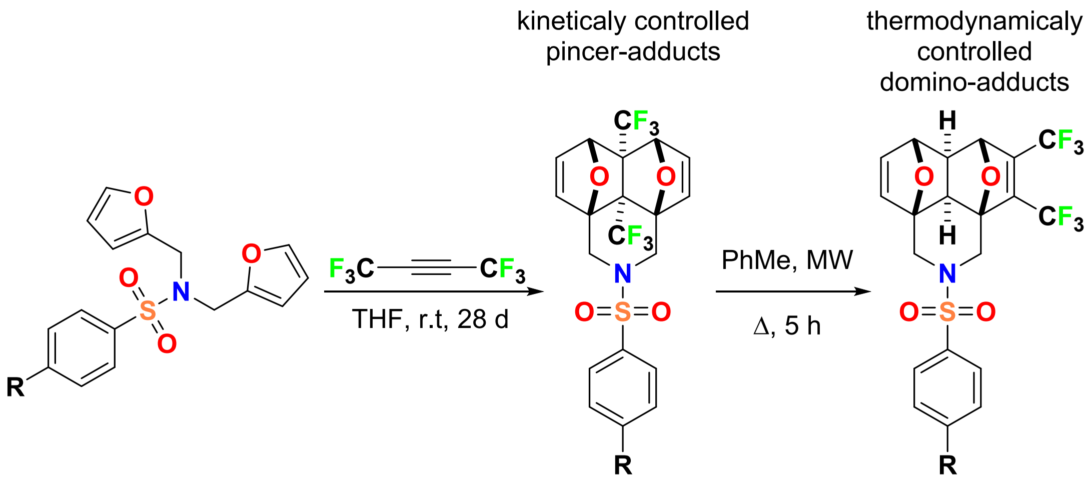

Scheme 1. Synthetic route to compounds **6–10** reported in this manuscript.

2. Methods

2.1 Experimental

All target substances **6−10** were synthesized according to the methods described early by our group[6,7] (see the ESI) based on sulfonamides **1−5**. The latest compounds were prepared by means of acylation of *bis*-(*N,N)*-furfurylamine by a series of commercially available sulfochlorides in the presence of an equimolar amount of triethylamine and a catalytic amount of DMAP according the classical procedure. It should be noted that the use of absolute solvent (THF) and pure starting sulfochlorides (which hydrolyze quickly in air) lead to the highest yields of sulfonamides **1−5** (81−99%).

The reaction between *bis*-dienes (sulfonamides, **1−5**) and hexafluorobutyne-2 was carried out under kinetically controlled conditions in sealed flasks in THF (abs.). At that, gaseous perfluorobutyne was previously condensed at −70 °C into an ampule filled with a solution of an appropriate sulfonamide. In preliminary experiments the ratio of *bis*-diene (**1−5**) / alkyne was varied from 1:1 to 1:1.4, which did not significantly affect both the yield of the cycloadducts (**6a−10a**) and the composition of the reaction mixtures. Therefore, in subsequent experiments the ratio of 1:1.1 was used everywhere. THF was chosen as a solvent due to its lower toxicity and, which is more important, rather low melting point. Under these conditions, all reactions were kept for around a month at r.t. with periodical shaking of an ampule. The composition of the obtained reaction mixtures was determined by Nuclear Magnetic Resonance (^{1}H NMR) spectroscopy after gentle evaporation of the solvent. The composition of crude reaction mixtures based on ^{1}H NMR data are given in Table 1.

View Article Online
DOI: 10.1039/D0NJ04328A

Table 1. Ratio and yields of adducts **6a−10a** and **6b−10b** obtained under conditions of kinetic or thermodynamic control.

Entry	R	Ratio [a] of **a**/**b** (%)	Unreacted sulfonamide **1−5** (%)	Yield of isolated **6a−10a** [b] (%)	Yield of isolated **6b−10b** [b,c] (%)
6	**Me**	79/4	17	75	72
7	**F**	79/4	17	70	70
8	**Cl**	89/5	6	77	78
9	**Br**	92.5/7	0.5	90	88
10	**I**	75/7	18	74	82

[a] Ratio of **a**/**b** is given according to the ^{1}H NMR analysis of the crude reaction mixtures obtained after solvent evaporation. [b] Isolated yields after recrystallization or column chromatography. [c] Domino-adducts **6b−10b** were obtained by heating of pincer-adducts **6a−10a** in toluene at 120 °C for 5 h under microwave (MW) irradiation.

As the data of Table 1 shows for the kinetically controlled conditions, the tandem [4+2] cycloaddition occurs chemoselectively in the most cases. This leads to mixtures of kinetically (pincer-adducts **6a−10a**) and thermodynamically (domino-adducts **6b−10b**) controlled products with small admixture of the initial sulfonamides (**1−5**) in the ratio of the main products **a**/**b** varying from 92/7 to 75/7.

After the solvent evaporation, the mixtures were crystallized in order to obtain pure pincer-adducts **6a−10a**. For further purification, a column chromatography on SiO_2 was performed when necessary. It should be noted that the use of column chromatography was a non-convenient purification method due to irreversible sorption of a part of the products on silica gel.

The rearrangement of pincer-adducts **6a−10a** into domino-products **6b−10b** proceeds at 120 °C in toluene under MW irradiation conditions. Toluene was chosen as a solvent due to its inertness and relatively low volatility. An attempt to carry out the process by refluxing pincer-adducts **6a−10a** in toluene or *o*-xylene for 2−3 h leads to a mixture of kinetically (**a**) and thermodynamically (**b**) controlled products. When the reaction time was increased up to 10 h, a significant decomposition of starting compounds and/or products was observed. Under MW conditions the corresponding adducts **6b−10b** were obtained in good yields (see Table 1) as white needles.

It is important to note, that the procedure of crystal growing for X-ray appeared to be a non-trivial task and specific conditions for each sample were needed. Unfortunately, after countless attempts, we were unable to obtain crystals of compound **10b** suitable for X-ray structural analysis.

DOI: 10.1039/D0NJ04328A

2.2 X-ray analysis

X-ray diffraction data for **6a**,**b**, **7a**,**b**, **8a**, **9a** and **10a** were collected on a three-circle Bruker Kappa APEX-II CCD diffractometer (MoK_{α}-radiation, graphite monochromator, φ and ω scan mode) and corrected for absorption using the *SADABS* program.[13] The data were indexed and integrated using the *SAINT* program.[14]

X-ray diffraction data for **8b** and **9b** were collected at the 'Belok' beamline (λ = 0.79313 Å) of the Synchrotron Radiation Source at the National Research Center "Kurchatov institute". In total, 720 frames were collected with an oscillation range of 1.0° in the φ scanning mode using two different orientations for each crystal. The semi-empirical correction for absorption was applied using the *Scala* program.[15] The data were indexed and integrated using the utility *iMOSFLM* from the CCP4 software suite.[16] For details, see Tables 2 and 3.

The structures were solved by intrinsic phasing modification of direct methods[17] and refined by a full-matrix least-squares technique on F^2 with anisotropic displacement parameters for all non-hydrogen atoms. The both CF_3-groups in **7b**, **8a** and **10a** and one of the two CF_3-groups in **8b** and **9b** are disordered over two sites each. The compound **8b** represented a non-merohedral twin. The absolute stereochemistry of pentacycles **7b**, **8b** and **9b** were objectively determined by the refinement of Flack parameter which has become equal to 0.08(8), 0.22(4) and 0.041(5), respectively. The hydrogen atoms were placed in calculated positions and refined within the riding model with fixed isotropic displacement parameters [$U_{iso}(H) = 1.5U_{eq}(C)$ for the methyl groups and $1.2U_{eq}(C)$ for the other groups]. All calculations were carried out using the SHELXTL program.[18,19]

Crystallographic data for **6a**,**b**, **7a**,**b**, **8a**,**b**, **9a**,**b** and **10a** have been deposited with the Cambridge Crystallographic Data Center, CCDC 2023800−2023808, respectively. Copies of this information may be obtained free of charge from the Director, CCDC, 12 Union Road, Cambridge CB2 1EZ, UK (fax: +44 1223 336033; e-mail: deposit@ccdc.cam.ac.uk or www.ccdc.cam.ac.uk).

Table 2. Crystal data and structure refinement for pincer-adducts **6a−10a**.

View Article Online
DOI: 10.1039/D0NJ04328A

Compound	**6a**	**7a**	**8a**	**9a**	**10a**
Empirical formula	$C_{21}H_{17}F_6NO_4S$	$C_{20}H_{14}F_7NO_4S$	$C_{20}H_{14}ClF_6NO_4S$	$C_{20}H_{14}BrF_6NO_4S$	$C_{20}H_{14}F_6INO_4S$
fw	493.42	497.38	513.83	558.29	605.28
T, K	100(2)	296(2)	296(2)	100(2)	296(2)
Crystal size, mm	0.40×0.44×0.50	0.32×0.40×0.44	0.32×0.44×0.50	0.34×0.36×0.40	0.40×0.42×0.50
Crystal system	Monoclinic	Monoclinic	Monoclinic	Monoclinic	Monoclinic
Space group	$P2_1/c$	$P2_1/c$	$P2_1/c$	$P2_1/c$	$P2_1/c$
a, Å	11.8375(3)	12.3306(4)	12.1445(5)	12.1236(3)	12.3934(3)
b, Å	15.1552(4)	10.6264(3)	15.3437(6)	15.5201(4)	16.1660(4)
c, Å	10.8340(3)	15.1459(4)	10.8727(4)	10.6655(3)	10.9810(2)
α, °	90	90	90	90	90
β, °	100.296(2)	99.930(1)	101.776(1)	101.754(1)	106.052(1)
γ, °	90	90	90	90	90
V, Å^3	1912.32(9)	1954.84(10)	1983.39(13)	1964.73(9)	2114.28(8)
Z	4	4	4	4	4
d_c, g·cm^{-3}	1.714	1.690	1.721	1.887	1.902
$F(000)$	1008	1008	1040	1112	1184
μ, mm^{-1}	0.260	0.262	0.385	2.286	1.695
θ range, °	4.14-30.00	3.84-30.00	4.34-30.00	4.12-35.00	4.15-30.00
Index range	$-16 \le h \le 16$ $-21 \le k \le 21$ $-15 \le l \le 12$	$-15 \le h \le 17$ $-14 \le k \le 13$ $-21 \le l \le 18$	$-17 \le h \le 16$ $-21 \le k \le 17$ $-10 \le l \le 15$	$-19 \le h \le 19$ $-23 \le k \le 25$ $-17 \le l \le 17$	$-17 \le h \le 17$ $-22 \le k \le 22$ $-14 \le l \le 15$
No. of reflections collected	18621	31844	27385	70216	28570
No. of unique reflections, R_{int}	5544, 0.033	5677, 0.028	5767, 0.028	8629, 0.032	6152, 0.019
No. of reflections with $I > 2\sigma(I)$	4668	4082	4235	7430	4816
No. of parameters refined	299	298	318	298	318
R_1 ($I > 2\sigma(I)$)	0.034	0.043	0.040	0.024	0.042
wR_2 (all data)	0.092	0.122	0.108	0.063	0.111
GOF on F^2	1.021	1.041	1.020	1.041	1.041
T_{min}; T_{max}	0.840; 0.903	0.862; 0.921	0.839; 0.887	0.438; 0.510	0.502; 0.550
Extinction coefficient	–	–	–	–	–
$\Delta\rho_{max}$; $\Delta\rho_{min}$, eÅ^{-3}	0.496; -0.381	0.290; -0.455	0.358; -0.472	0.537; -0.492	1.563; -1.693

View Article Online
DOI: 10.1039/D0NJ04328A

Table 3. Crystal data and structure refinement for domino-adducts **6b−9b**.

Compound	**6b**	**7b**	**8b**	**9b**
Empirical formula	$C_{21}H_{17}F_6NO_4S$	$C_{20}H_{14}F_7NO_4S$	$C_{20}H_{14}ClF_6NO_4S$	$C_{20}H_{14}BrF_6NO_4S$
fw	493.42	497.38	513.83	558.28
T, K	100(2)	296(2)	100(2)	100(2)
Crystal size, mm	0.12×0.32×0.40	0.04×0.10×0.40	0.15×0.20×0.22	0.08×0.12×0.15
Crystal system	Orthorhombic	Monoclinic	Monoclinic	Monoclinic
Space group	*P*bca	$P2_1$	$P2_1$	$P2_1$
a, Å	9.6619(4)	12.1261(11)	12.8242(18)	13.111(3)
b, Å	19.6122(8)	5.3231(5)	5.1860(7)	5.1760(10)
c, Å	21.6230(9)	15.7434(14)	14.912(2)	14.827(3)
α, °	90	90	90	90
β, °	90	99.951(6)	99.717(18)	99.291(10)
γ, °	90	90	90	90
V, Å^3	4097.4(3)	1000.92(16)	977.5(2)	993.0(4)
Z	8	2	2	2
d_c, g·cm^{-3}	1.600	1.650	1.746	1.867
F(000)	2016	504	520	556
μ, mm^{-1}	0.243	0.256	0.521	2.965
θ range, °	4.09-30.00	3.41-25.00	1.55-26.01	1.55-30.98
Index range	$-13 \leq h \leq 13$ $-27 \leq k \leq 27$ $-30 \leq l \leq 30$	$-14 \leq h \leq 14$ $-6 \leq k \leq 6$ $-18 \leq l \leq 18$	$-14 \leq h \leq 13$ $-5 \leq k \leq 5$ $-16 \leq l \leq 16$	$-16 \leq h \leq 17$ $-6 \leq k \leq 6$ $-16 \leq l \leq 19$
No. of reflections collected	49338	9370	2713	7742
No. of unique reflections, R_{int}	5967, 0.055	3091, 0.051	2713, 0.049	4498, 0.033
No. of reflections with $I > 2\sigma(I)$	4538	2332	2624	4256
No. of parameters refined	299	320	346	345
R_1 ($I > 2\sigma(I)$)	0.043	0.087	0.091	0.056
wR_2 (all data)	0.121	0.254	0.222	0.131
GOF on F^2	1.029	1.063	1.057	1.048
T_{min}; T_{max}	0.895; 0.971	0.905; 0.990	0.884; 0.919	0.636; 0.770
Extinction coefficient	—	—	—	0.041(4)
$\Delta\rho_{max}$; $\Delta\rho_{min}$, eÅ^{-3}	0.549; −0.344	0.740; −0.480	0.761; −1.073	0.829; −1.162

2.3. Hirshfeld surface calculations

View Article Online
DOI: 10.1039/D0NJ04328A

The Hirshfeld surfaces (HSs) and their associated two-dimensional fingerprint (FP) plots[20−23] were used to understand the nature of intermolecular interactions that are responsible of the packing stabilization and to quantify the contribution of different contact to the total Hirshfeld surface area. The normalized contact distance (d_{norm}) is calculated taking into account the values of d_e (the distance between the HS and external molecule), d_i (the distance between the HS and inside molecule) and van der Waals (vdW) radii of the atoms (r_i^{vdW}) or (r_e^{vdW}). The value of d_{norm} calculated with equation (1) allows us to identify the different regions participating in the intermolecular interactions.

$$d_{norm} = \frac{d_i - r_i^{vdW}}{r_i^{vdW}} + \frac{d_e - r_e^{vdW}}{r_e^{vdW}} \quad (1)$$

The HSs and their associated FP plots were generated using the CrystalExplorer17 program,[24] using the crystallographic information files obtained from the crystal structure determination. The d_{norm} surfaces were mapped over a fixed color scale of −0.075 au (red) to 0.75 au (blue). The 2D fingerprint plots were displayed using the translated 0.6−2.4 Å range including reciprocal contacts.

2.4 Theoretical Methods

The energies of the complexes included in this study were computed at the PBE1PBE-D3/def2-TZVP level of theory by using the program Gaussian-16.[25] The interaction energy (or the binding energy in this work) ΔE, is defined as the energy difference between the multicomponent assembly and the sum of the energies of the monomers. The basis set superposition error has been corrected using the counterpoise method.[26] For the calculations we have used the Weigend def2-TZVP[27,28] basis set and the PBE0 DFT functional[29,30] and Grimme's D3 dispersion correction.[31] The MEP (Molecular Electrostatic Potential) surfaces calculations have been computed using Gaussian-16 software at the PBE0-D3/def2-TZVP level of theory. The NCIPlot[32] index and QTAIM analyses have been performed using the PBE0-D3/def2-TZVP wave function and the AIMAll program.[33] For the calculations we have used the X-ray geometries because we are interested in studying the interactions as they stand in the solid state. This methodology[34] and level of theory[35] used in this work has been previously used to analyze a variety of interactions in the solid state.

3. RESULTS AND DISCUSSION

3.1. Description of the structures

The structures of the products of the tandem [4+2]/[4+2] cycloaddition **6a**,**b**, **7a**,**b**, **8a**,**b**, **9a**,**b** and **10a** were unambiguously established by X-ray diffraction study and are shown in Figure 1 along with the atomic numbering schemes. It is important to point out that compounds **6a** and

8a−10a (Table 2) are isostructural to each other, and compounds **7b−9b** are isostructural to each other as well (see Table 3).

View Article Online
DOI: 10.1039/D0NJ04328A

DOI: 10.1039/D0NJ04328A

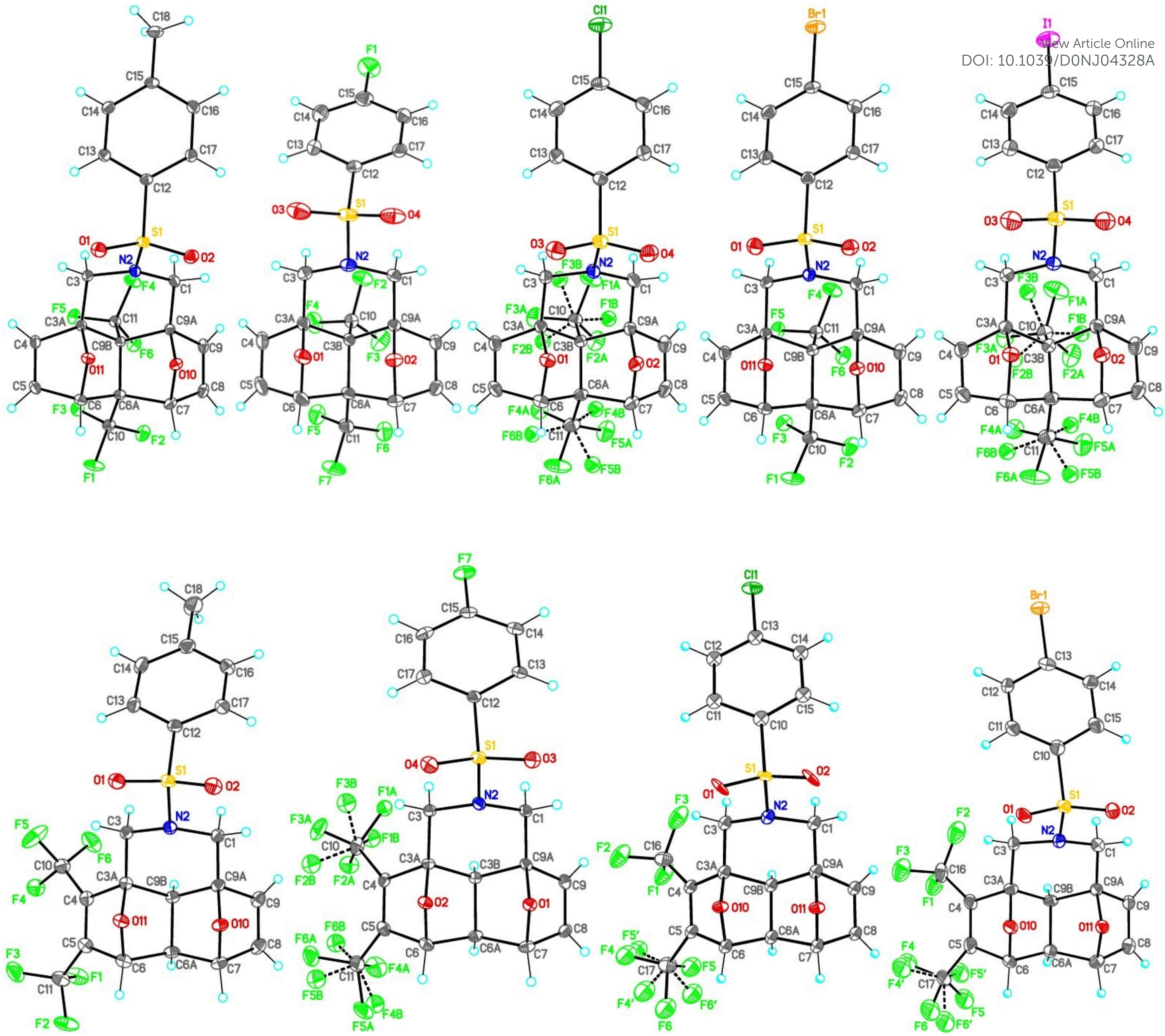

Figure 1. Molecular structures of pincer-adducts **6a−10a** (top) and domino-adducts **6b−9b** (bottom).

Compounds **6a**,**b**, **7a**,**b**, **8a**,**b**, **9a**,**b** and **10a** comprise fused pentacyclic 3a,6:7,9a-diepoxybenzo[*de*]isoquinoline system. The six-membered piperidine ring adopts the typical *chair* conformation, and the four five-membered rings – two furan and two dihydrofuran ones have the usual *envelope* conformation. In all compounds, the sulfonamide nitrogen atoms have a flattened pyramidalized geometry (sum of the bond angles is equal to 358.4(3), 347.7(3), 347.4(3), 350(2), 358.0(3), 352(5), 357.0(2), 351(2) and 354.3(6)°, respectively), and therefore, are close to sp^2-hybridization. The bulk *N*-phenylsulfonyl substituent occupies the more sterically favorable pseudo-equatorial position in the piperidine ring.

The molecules of **6a−10a** possess four asymmetric centers at the C3A, C6, C7 and C9A carbon atoms and can have potentially sixteen diastereomers. The crystals of **6a−10a** are racemic and consists of enantiomeric pairs with the following relative configuration of the centers: ***rac***-3A***RS***, 6***SR***,7***RS***,9A***SR***.

The molecules of **6b−9b** possess six asymmetric centers at the C3A, C6, C6A, C7, C9A and C9B carbon atoms and can have potentially sixty-four diastereomers. The crystal of **6b** is racemic and consists of enantiomeric pairs with the following relative configuration of the centers: ***rac***-3A***SR***,6***RS***,6A***RS***,7***RS***,9A***SR***,9B***RS***. The crystals of **7b−9b** are chiral and consists of diastereomers with the following absolute configuration of the centers: 3A***S***,6***R***,6A***R***,7***R***,9A***S***,9B***R***.

In the crystals of **6a** and **8a−10a**, despite their isostructurality, molecules form different hydrogen bonding and secondary interactions (Figure 2, Table 4). That is, in **6a** and **8a**, the molecules are linked by weak C—H···F and C—H···O hydrogen bonds, generating the final three-dimensional framework. Unlike to **6a** and **8a**, the molecules of **9a** are bound into three-dimensional framework not only by the weak C—H···F and C—H···O hydrogen bonds, but also additional weak secondary Br1···F1 [3.350(1) Å, symmetry: -x, -1/2-y, 1/2+z] interactions. The molecules of **10a** are arranged at van-der-Waals distances.

In the crystal of **6b**, the molecules are linked by weak C—H···F and C—H···O hydrogen bonds as well as secondary F1···F2 [2.766(2) Å, symmetry: -1/2+x, y, ½-z] interactions into three-dimensional framework (Figure 3, Table 4). In the crystal of **7a**, the molecules form chains toward [010] by the weak C—H···O hydrogen bonds (Figure 4, Table 4). The chains are bound by weak C—H···F hydrogen bonds into three-dimensional framework (Table 4). In the crystal of **7b**, the molecules are linked by weak C—H···O hydrogen bonds as well as weak secondary F···F interactions, thus forming the three-dimensional framework (Figure 5, Table 4), whereas, in the crystals of **8b** and **9b**, the molecules are bound by the weak C—H···O hydrogen bonds as well as weak secondary F···F interactions, forming two-tier layers parallel to (001) (Figure 5, Table 4).

Table 4. Hydrogen bonds for **6a**,**b**, **7a**,**b**, **8a**,**b**, **9a**,**b** and **10a** [Å and °].

View Article Online
DOI: 10.1039/D0NJ04328A

D—H···A	d(D—H)	d(H···A)	d(D···A)	<(DHA)
Compound **6a**				
C3—H3B···F1[a]	0.99	2.43	3.3893(15)	161.9
C4—H4A···O1[b]	0.95	2.43	3.2371(16)	142.4
C13—H13A···O2[b]	0.95	2.57	3.3619(16)	141.1
Compound **6b**				
C6—H6A···F1[c]	1.00	2.42	3.334(2)	151.1
C9—H9A···O11[d]	0.95	2.58	3.393(2)	143.1
C13—H13A···O1[e]	0.95	2.46	3.396(2)	169.4
C17—H17A···F1[f]	0.95	2.53	3.198(2)	127.0
C17—H17A···F2[f]	0.95	2.46	3.414(2)	177.1
Compound **7a**				
C3—H3A···F1[g]	0.97	2.43	3.273(2)	144.6
C8—H8···O2[a]	0.93	2.45	3.244(2)	142.8
Compound **7b**				
C3B—H3BA···O2[h]	0.98	2.38	3.350(11)	172.4
C13—H13A···O3[i]	0.93	2.57	3.436(13)	154.7
Compound **8a**				
C3—H3B···F6A[j]	0.97	2.52	3.448(2)	161.1
C4—H4···F6B[k]	0.93	2.47	3.201(10)	135.7
C4—H4···O3[l]	0.93	2.54	3.330(2)	142.6
C13—H13···O4[l]	0.93	2.59	3.274(2)	130.6
Compound **8b**				
C3—H3A···O1[h]	0.99	2.47	3.38(3)	153.1
C9B—H9B···O10[h]	1.00	2.34	3.32(3)	167.7
Compound **9a**				
C3—H3B···F1[a]	0.99	2.53	3.4951(12)	163.9
C4—H4A···O1[b]	0.95	2.51	3.2931(12)	140.1
C13—H13A···O2[b]	0.95	2.55	3.2084(12)	126.3
Compound **9b**				
C3—H3A···O1[h]	0.99	2.48	3.414(13)	157.2
C9B—H9B···O10[h]	1.00	2.32	3.296(12)	163.7
C15—H15···O2[m]	0.95	2.59	3.493(12)	157.9

Symmetry transformations used to generate equivalent atoms: [a] -x+1, y+1/2, -z+3/2; [b] x, -y+3/2, z+1/2; [c] x+1/2, y, -z+1/2; [d] x-1/2, -y+1/2, -z+1; [e] -x+1, -y, -z+1; [f] x, -y+1/2, z+1/2; [g] -x+2, -y+1, -z+1; [h] x, y+1, z; [i] -x+1, y+1/2, -z+1; [j] -x, y+1/2, -z+1/2; [k] -x, -y+1, -z; [l] x, -y+3/2, z-1/2; [m] -x+1, y+1/2, -z.

View Article Online
DOI: 10.1039/D0NJ04328A

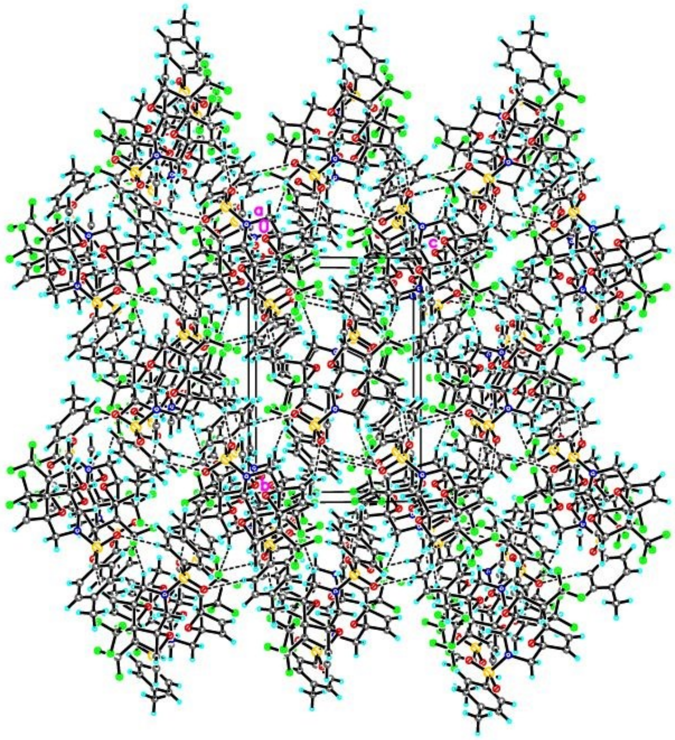

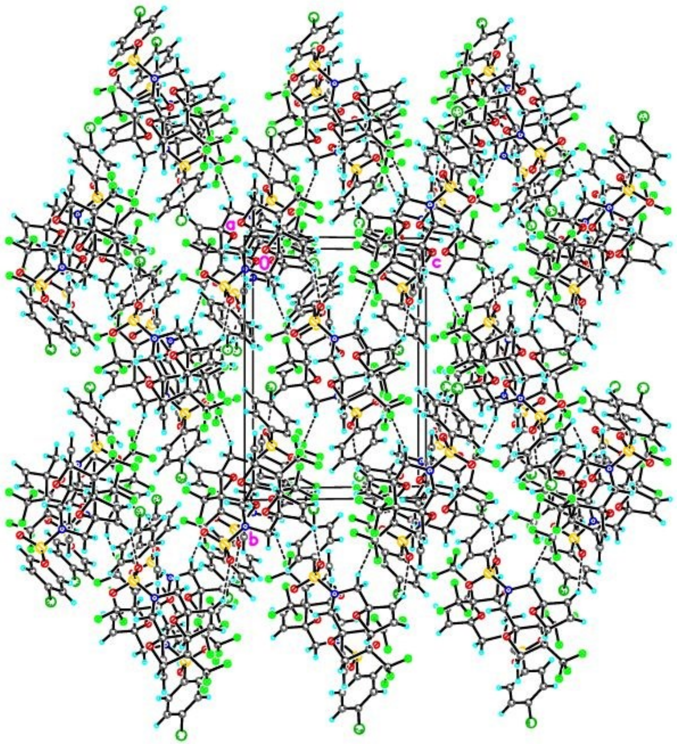

View Article Online
DOI: 10.1039/D0NJ04328A

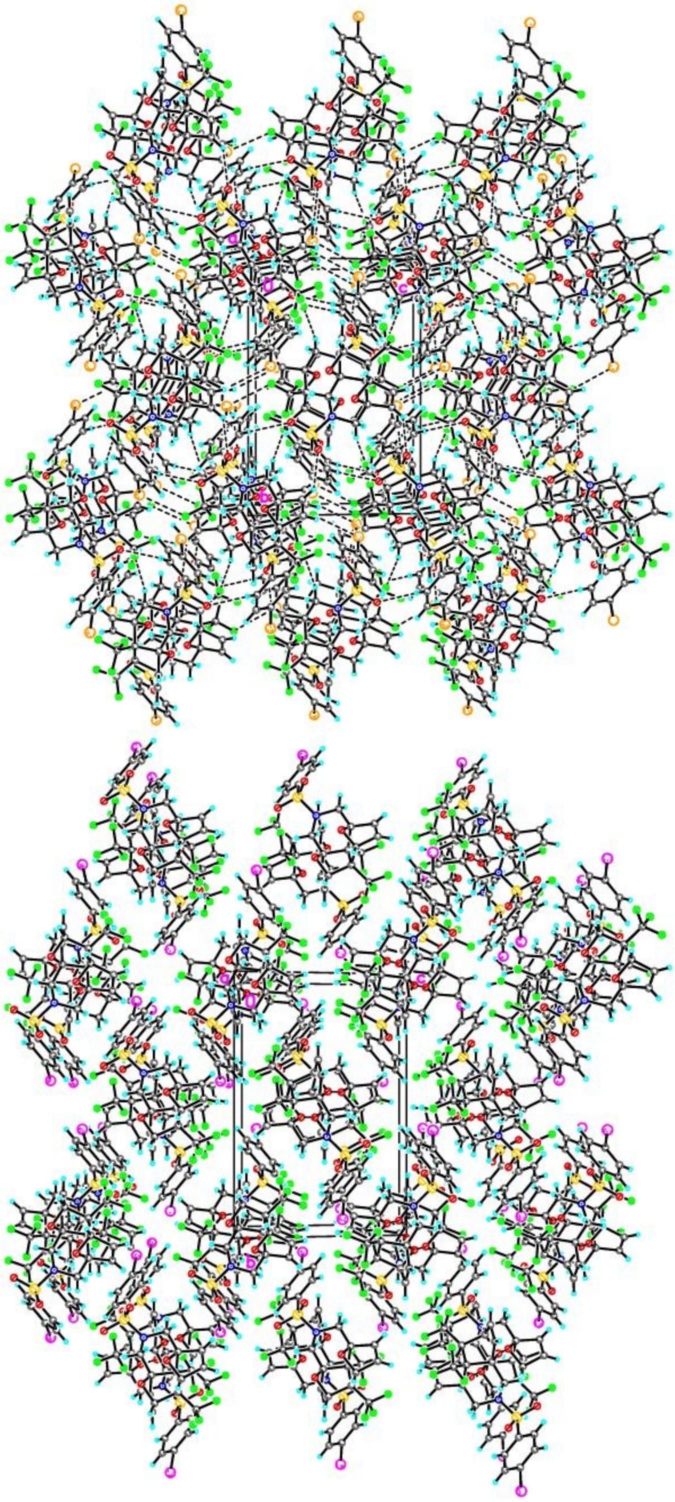

Figure 2. Crystal structures of compounds **6a** and **8a−10a** along the crystallographic *a* axis. The intermolecular C─H···O and C─H···F hydrogen bonds as well as secondary Br···F interactions are depicted by dashed lines.

View Article Online
DOI: 10.1039/D0NJ04328A

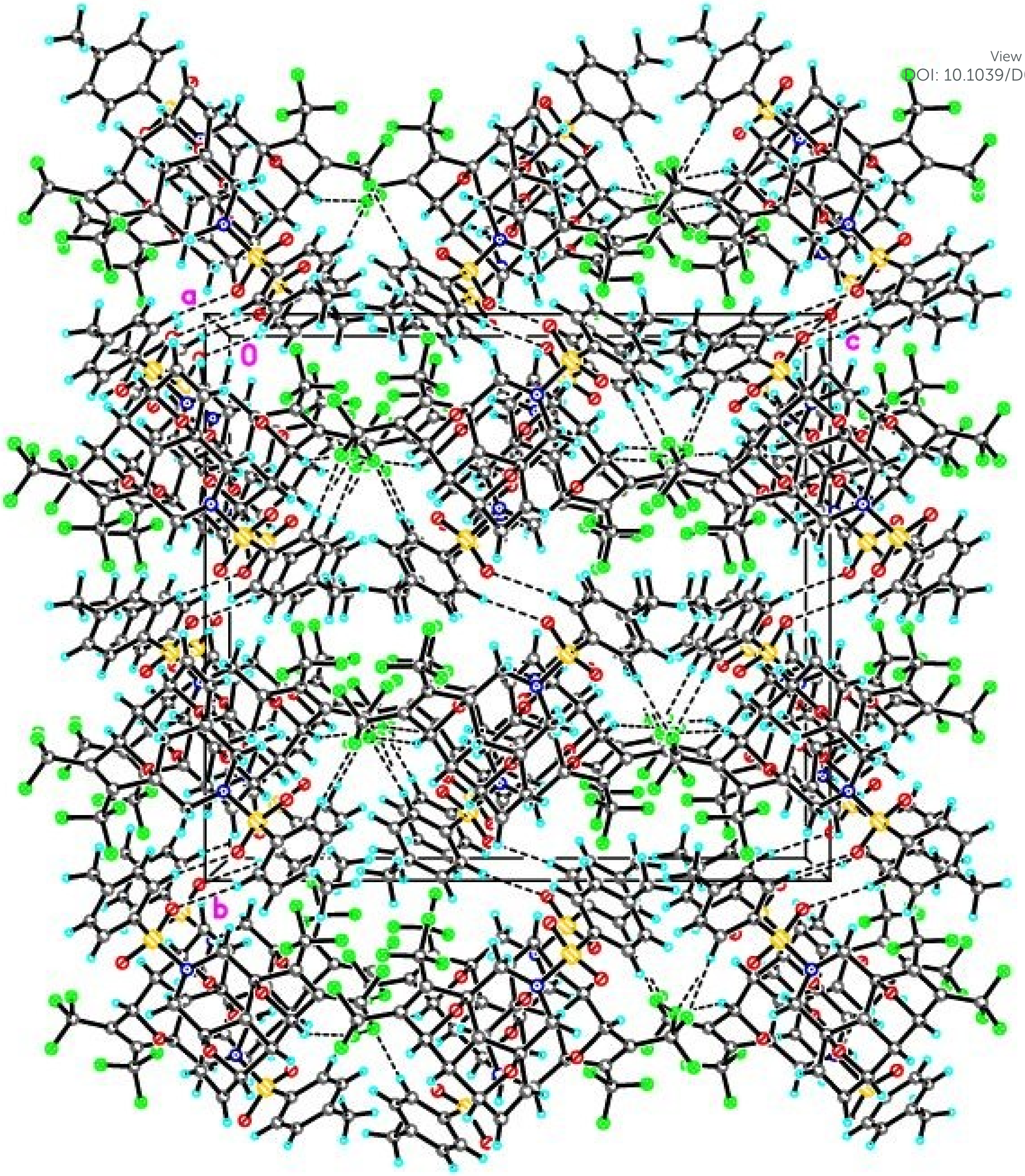

Figure 3. Crystal structure of compound **6b** along the crystallographic *a* axis. The intermolecular C─H···O and C─H···F hydrogen bonds interactions are depicted by dashed lines.

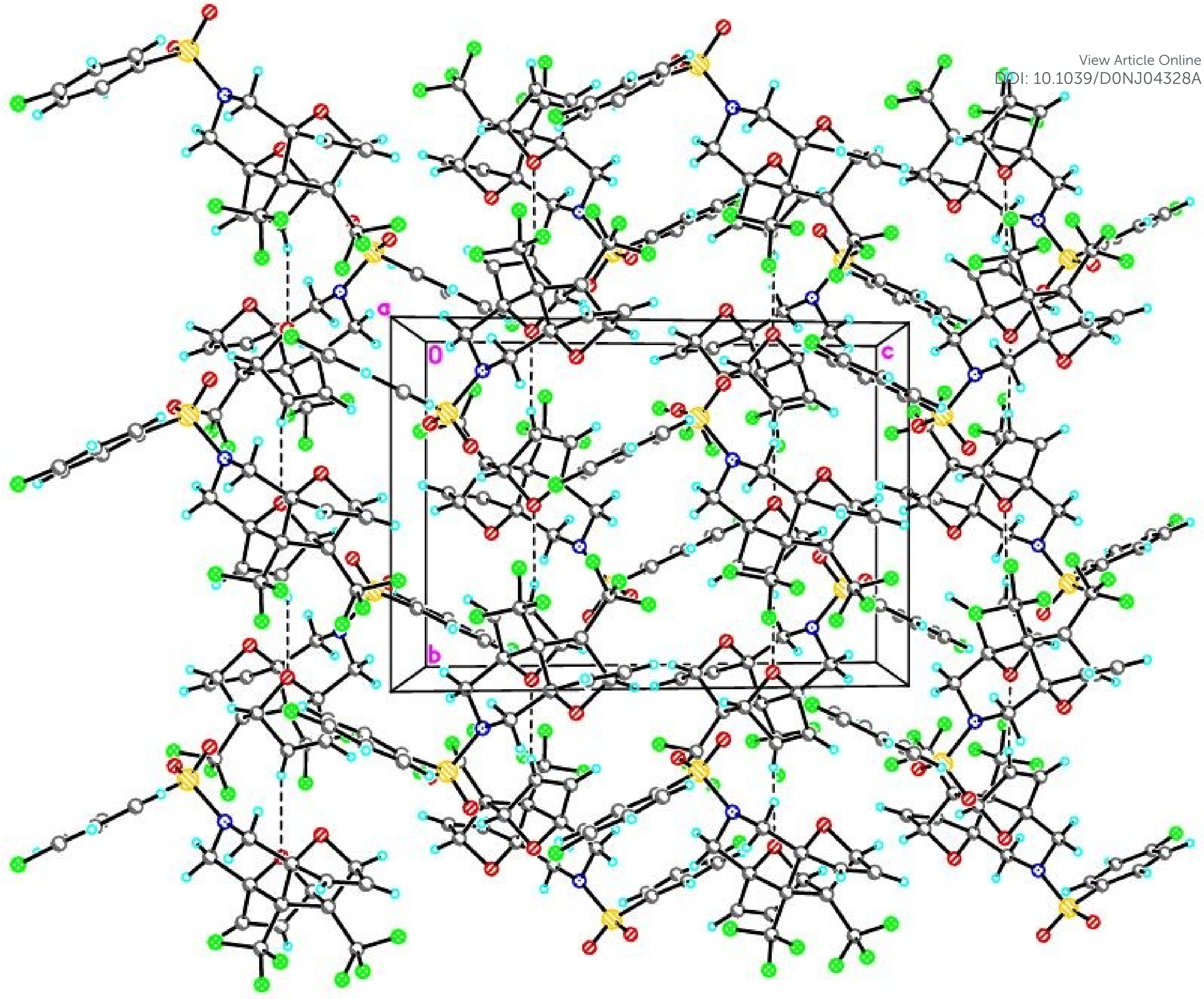

Figure 4. Crystal structure of compound **7a** along the crystallographic *a* axis. The intermolecular C─H···O hydrogen bonds are depicted by dashed lines.

View Article Online
DOI: 10.1039/D0NJ04328A

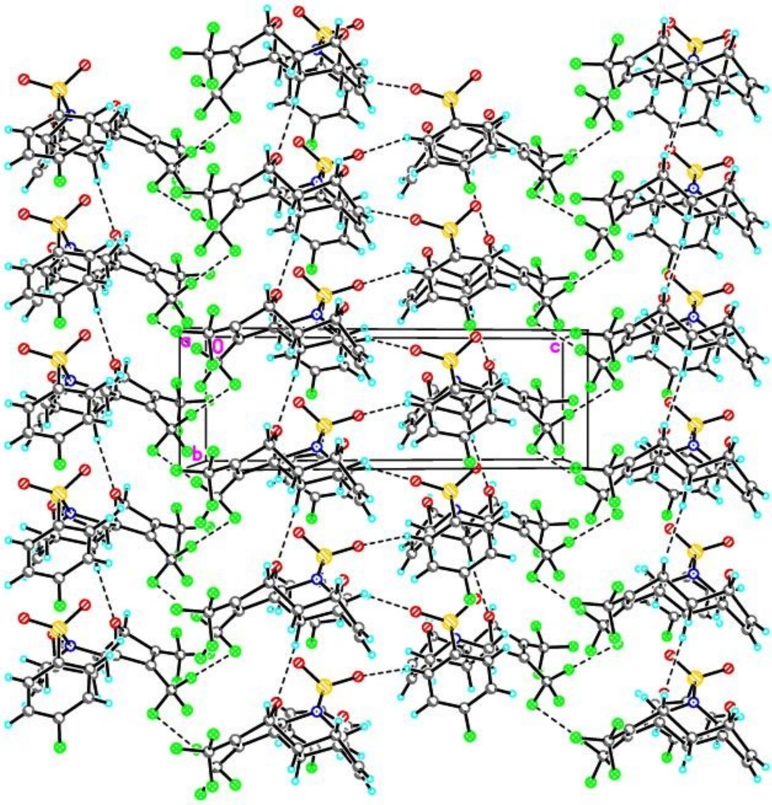

View Article Online
DOI: 10.1039/D0NJ04328A

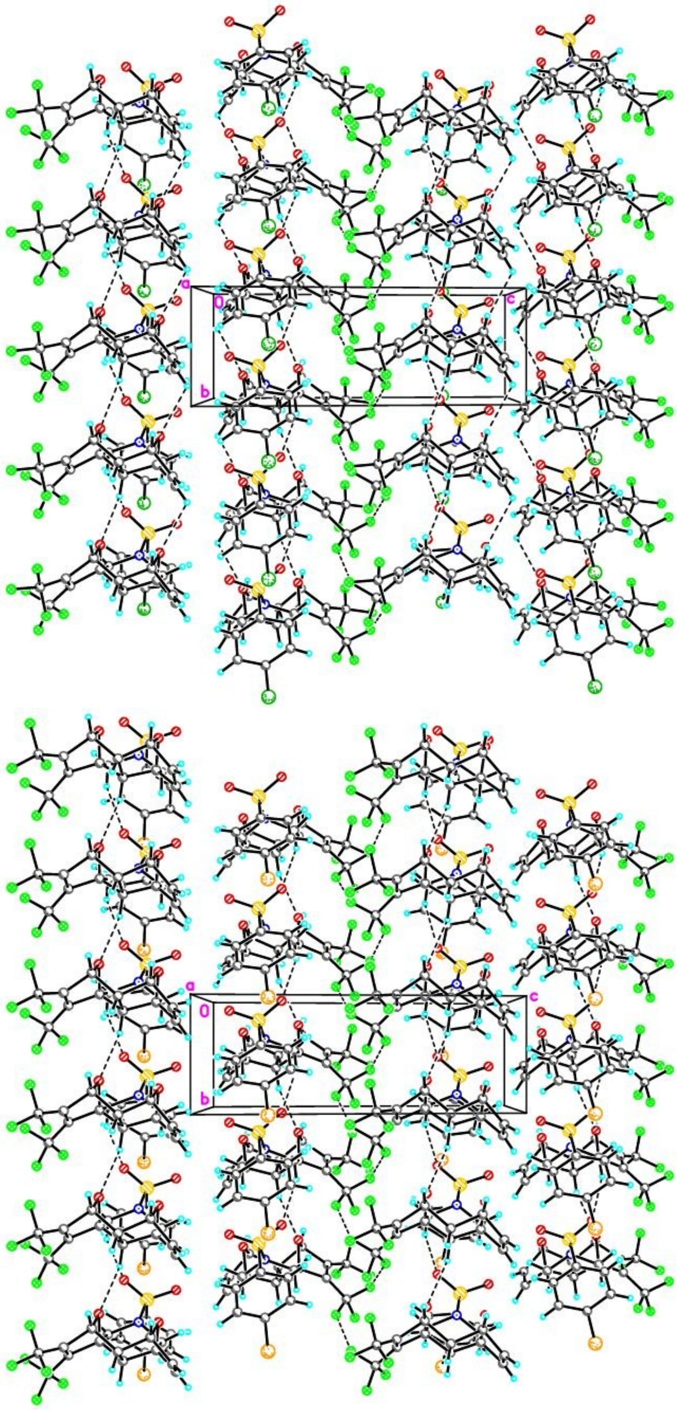

Figure 5. Crystal structures of compounds **7b–9b** along the crystallographic *a* axis. The intermolecular C–H···O hydrogen bonds and non-valent attractive F···F interactions are depicted by dashed lines.

A common feature of compounds **6b−9b** is the formation of 1D supramolecular chains in the solid state, as represented in Figure 6. The 1D assemblies are equivalent in the isostructural halide derivatives **7b−9b**. However, for the methyl derivative (**6b**) the 1D polymeric chain is different exhibiting a zig-zag arrangement of the monomers. In all cases C–H···O H-bonds are responsible for the formation of the 1D chains that are represented by black dashed lines in Figure 6.

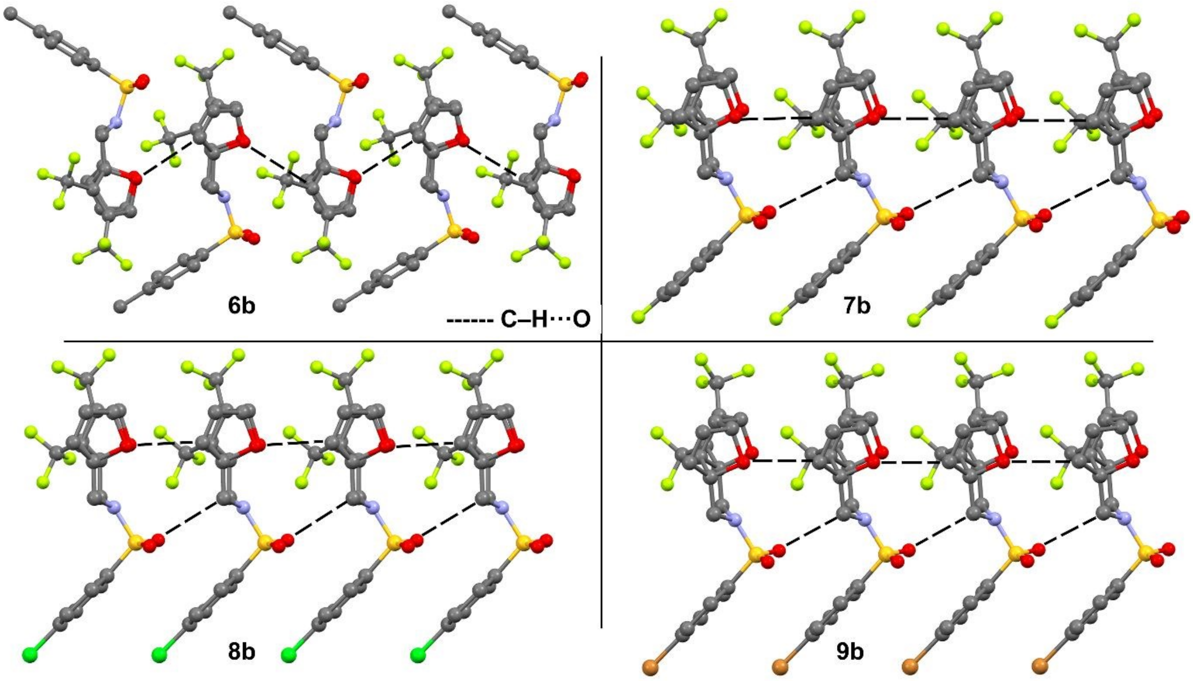

Figure 6. 1D supramolecular assemblies observed in the solid state of domino compounds **6b−9b**. H-atoms omitted for clarity, they are shown below in the DFT section

In contrast, pincer compounds form interesting self-assembled dimers in the solid state (see Figure 7) where in addition to C–H···O interactions, ancillary F···O contacts are present (see blue dashed lines). In some cases, the F···O distance is very similar to the sum of van der Waals radii (3.0 Å). The relevance of this uncommon halogen bonding interaction is further analyzed below in the theoretical study.

View Article Online
DOI: 10.1039/D0NJ04328A

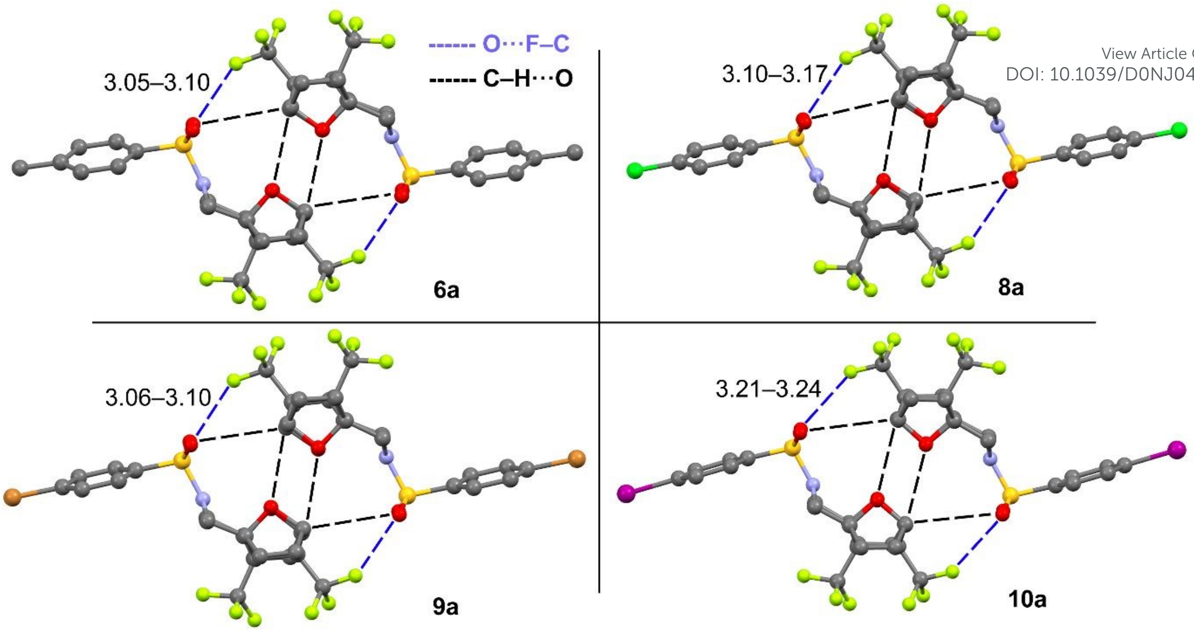

Figure 7. 1D supramolecular assemblies observed in the solid state of domino compounds **6a**, **8a**–**10a**. Distances in Å. H-atoms omitted for clarity, they are shown below in the DFT section.

3.2. Hirshfeld surface analysis

The Hirshfeld surfaces and two dimensional FP plots have been computed for investigating similarities and differences in the crystal packing of the series of nine structures under consideration. Figure 8 shows the HSs mapped over d_{norm} property for the compounds with domino and pincer type structures. The red spots on the surfaces represent distances shorter than sum of vdW radii and blue regions correspond to distances longer than sum of vdW radii. Figures 9 and 10 show the two dimensional fingerprint plots of domino and pincer structures, respectively. Hirshfeld surface analyses of compounds **6a**,**b** suggest that the structures of both compounds are stabilized by C-H···F, C-H···O, F···F, F···O and O···O non-covalent interactions. The red spots labelled 1, 3 and 5 in the HS of **6a** and 1 and 4 for **6a** are attributed to intermolecular C-H···F contacts, which can also be seen in the FP plots as a pair of symmetrical spikes at ($d_e + d_i$) ~ 2.3 Å for the former and ($d_e + d_i$) ~ 2.4 Å for the later interaction. The H···F/F···H interactions are dominant, with highest contributions of 30.0 and 31.4% for **6b** and **6a**, respectively. The presence of F2···F1 and F5···O1 contacts in the crystal packing of **6b** is evidenced by visible bright red areas labeled as 2 and 6, respectively in the d_{norm} surface (Figure 8). These contacts are visible in the 2D fingerprint plots contributing 5.3 and 4.8% to the total Hirshfeld surface area. The red spots labelled 4 and 7 and 2, 3 and 5 in the d_{norm} map of **6b** and **6a**, respectively are attributed to weak C-H···O hydrogen bonds. The proportions of H···O/O···H interactions comprise 20.3 and 20.6% of the total Hirshfeld surface area of **6b** and **6a**, respectively. Additionally, the crystal packing of **6a** is also stabilized by chalcogen O10···O11 interactions involving the *O*-atoms of the ether groups of two molecules. The distance O···O in this compound [d(O10···O11) = 3.016 Å] is slightly shorter than the sum of vdW radii (3.04 Å). These contacts are visible in the d_{norm} surface as a red spot labeled 6. The structure of **6b** is stabilized by C-H···π interactions, which are evident from a pair of "wings" in the top left and button right region of the FP plot (see Figure 9). These H···C/C···H contacts comprise 8.4% of total Hirshfeld surface area.

The Hirshfeld surfaces mapped over d_{norm} function for **7b** show two red areas labelled 1 and 2 associated to F4···F5 and F1···F3 halogen bonding interactions. These contacts are visible in the FP plot as broad spikes at around ($d_e + d_i$) ~ 2.6 Å, in accordance with the F···F distance of 2.647 and 2.886 Å for F1···F3 and F4···F5 contacts, respectively. These halogen bonds comprise 15.9% of the total HS area. The red regions located around the F7 and H6A atoms are attributed to weak C6A-H6A···F7 hydrogen bonds. These interactions are dominant and comprise 29.5% of total HS area. The crystal packing of **7b** is also stabilized by C-H···O hydrogen bonds, as can be shown in the red regions labeled 4, 5 and 6 in the d_{norm} surface, with 19.2% of contribution to the Hirshfeld surface area.

The white and red spots observed in the d_{norm} surface of **7a** labeled 1 and 2, respectively are associated to weak C-H···F hydrogen bonds involving the acceptors F7 and F5 of the CF_3 group. The larger red spots labeled 3 are attributed to C3-H3A···F1 involving the fluorine atom of the phenyl ring. The H···F/F···H interactions are represented as a pair of spikes at ($d_e + d_i$) ~ 2.3 Å in the FP plot, with a higher 34.5% contribution. The red spot labeled 4 in the HS mapped over d_{norm} function is associated to C-H···O hydrogen bonds. The supramolecular assembly of **7a** is also stabilized by lone pair O···π and C-H···C9 interactions. These contacts are visible in the Hirshfeld surfaces as red spots labeled 5 for the former and 6 for the later interaction.

In accordance with Hirshfed surface analysis, the crystal packing features of **8a** and **8b** are very different. The HSs mapped over d_{norm} property show red spots labeled 3 and 1 for **8b** and **8a**, respectively. These spots are associated to C3-H3B···F2 and C3-H3B···F6A for the former and the later compound, respectively. The H···F/F···H contacts are evident in the FP plots (Figures 9 and 10) as broad spikes at around ($d_e + d_i$) ~ 2.4 Å, which comprise 21.4 and 31.3% of the total Hirshfeld surface area of **8b** and **8a**, respectively. The crystal structure of **8b** is also stabilized by C6-H6···Cl1 interactions, which are visible in the d_{norm} surface as red spots labeled 4. The deep red visible spots labeled 5−8 and 2−4 for **8b** and **8a**, respectively are indicative of C-H···O hydrogen bonds. The crystal packing of **8b** exhibit F···F interactions involving F5 with F6 and F2 with F3. These interactions appear as large deep red spots in the d_{norm} surface, labeled 1 and 2 (Figure 8). These interactions are also observed in the FP plot as symmetric pair of broad spikes at ($d_e + d_i$) ~ 2.6 Å, in accordance with the F···F distance of 2.657 and 2.651 Å for F5···F6 and

F2···F3 interactions, respectively. The proportion of F···F contacts comprises 13.0% of the total HS area for each molecule.

View Article Online
DOI: 10.1039/D0NJ04328A

Similarly to **8b**, the crystal packing of **9b** is also stabilized by intermolecular F5···F6 and F2···F3 interactions involving the fluorine atoms of the CF_3 groups. The contacts are visible in the d_{norm} surface as deep red regions labeled 1 and 2. The decomposed FP plot of the mentioned compound shows a broad spike centered at $(d_e + d_i) \sim 2.6$ Å with 12.5% contribution to the HS area. The white spots labeled 3 in the d_{norm} map are attributed to C6-H6···Br1 [d(H6···Br1)= 2.962 Å] and C7-H7···Br1 [d(H7···Br1)= 3.023 Å]. These interactions are visible in the FP plot as two sharp spikes with $(d_e + d_i) \sim 2.9$ Å and a contribution of 9.9 % of the total HS area. The red regions labeled 5−8 are attributed to C-H···O contacts, which contribute 18.0% to the total HS area. The crystal packing of **9a** is further stabilized by weak C-H···F hydrogen bonds involving the F1 and F6 atoms of the CF_3 groups and the H-atoms H3B and H16A. The d_{norm} HS of **9a** (Figure 8) shows two red spots labeled 1 and 2, associated to two different C-H···F hydrogen bonds. These interactions are represented as a pair of spikes at $(d_e + d_i) \sim 2.35$ Å with a high 29.8% contribution. The C-H···O hydrogen bonds are viewed by the bright red areas labeled 3−5 in the d_{norm} surfaces. The proportion of H···O/O···H interactions comprises 18.7% of the total Hirshfeld surface area.

View Article Online
DOI: 10.1039/D0NJ04328A

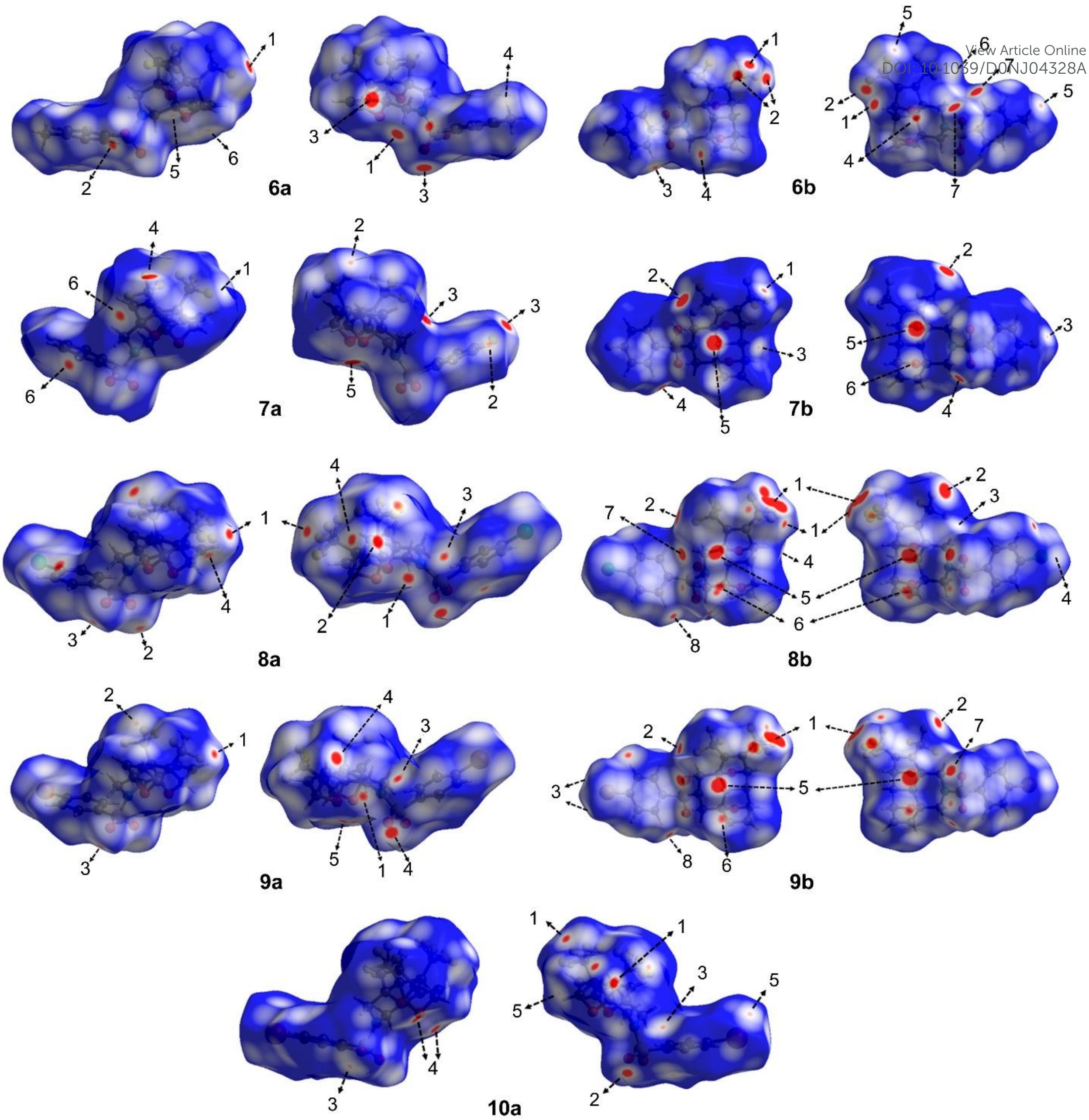

Figure 8. Hirshfeld surfaces mapped over d_{norm} function for all compounds. The second molecule is rotated by 180° around the vertical axis of the plot. The labels are discussed in the main text.

In the structure of **10a**, the H···F/F···H contacts labeled 1 in Figure 8 are dominant, appearing as two larger deep red spots around the H3B and F6A atoms attributed to C3-H3B···F6A hydrogen bonds. These interactions are also observed as sharp symmetrical spikes with short ($d_e + d_i$) ~ 2.4 Å with a higher contribution of 32.0% to the total Hirshfeld surface. The presence of C-H···O hydrogen bonds in the crystal assembly of **10a** is evident by the presence of the red spots labeled 2 and 3 in the d_{norm} surface (Figure 8). The H···O/O···H interactions comprise 17.8% of the total HS area. The supramolecular assembly of **10a** also includes I1···C5 and chalcogen O1···O2 intermolecular interactions, which are visible in the HSs mapped over d_{norm} property as red spots labeled 5 and 4, respectively. The calculations of HSs reveal that in all compounds, the van der Waals H···H contacts contribute to the crystal stabilization in the wide range of 15.6–20.5%, as result of the differences in the relative content of hydrogen atoms. The importance of this type of homopolar C–H···H–C interactions have been described in many systems and studied theoretically.[36] For instance, the influence of the dihydrogen bonding C–H···H–C on the solid state geometry of transition metal complexes has been evidenced both experimental and theoretically.[37]

View Article Online
DOI: 10.1039/D0NJ04328A

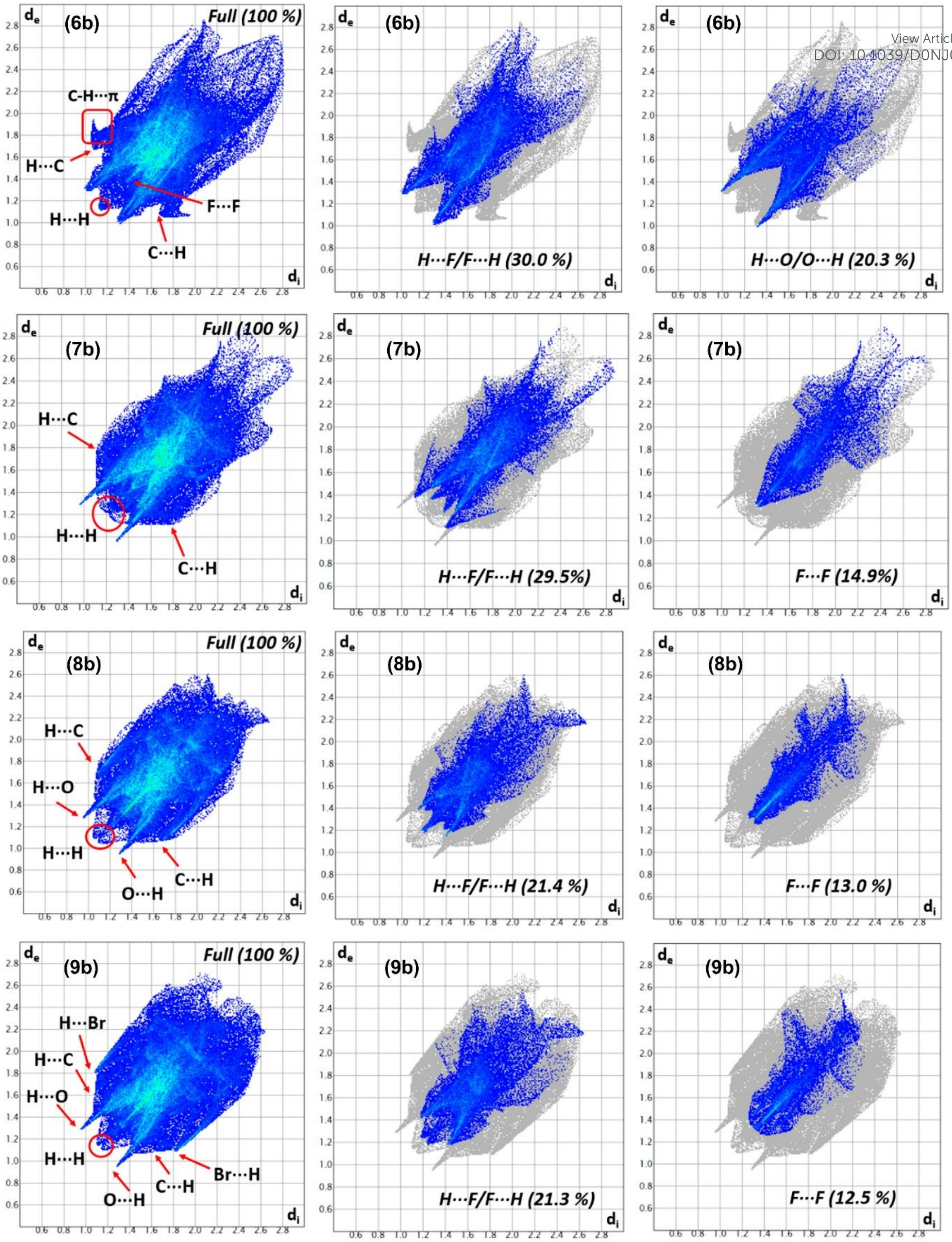

Figure 9. Full and decomposed two dimensional fingerprint plots for domino-adducts (**6b−9b**) showing the spikes of the main intermolecular interactions.

View Article Online
DOI: 10.1039/D0NJ04328A

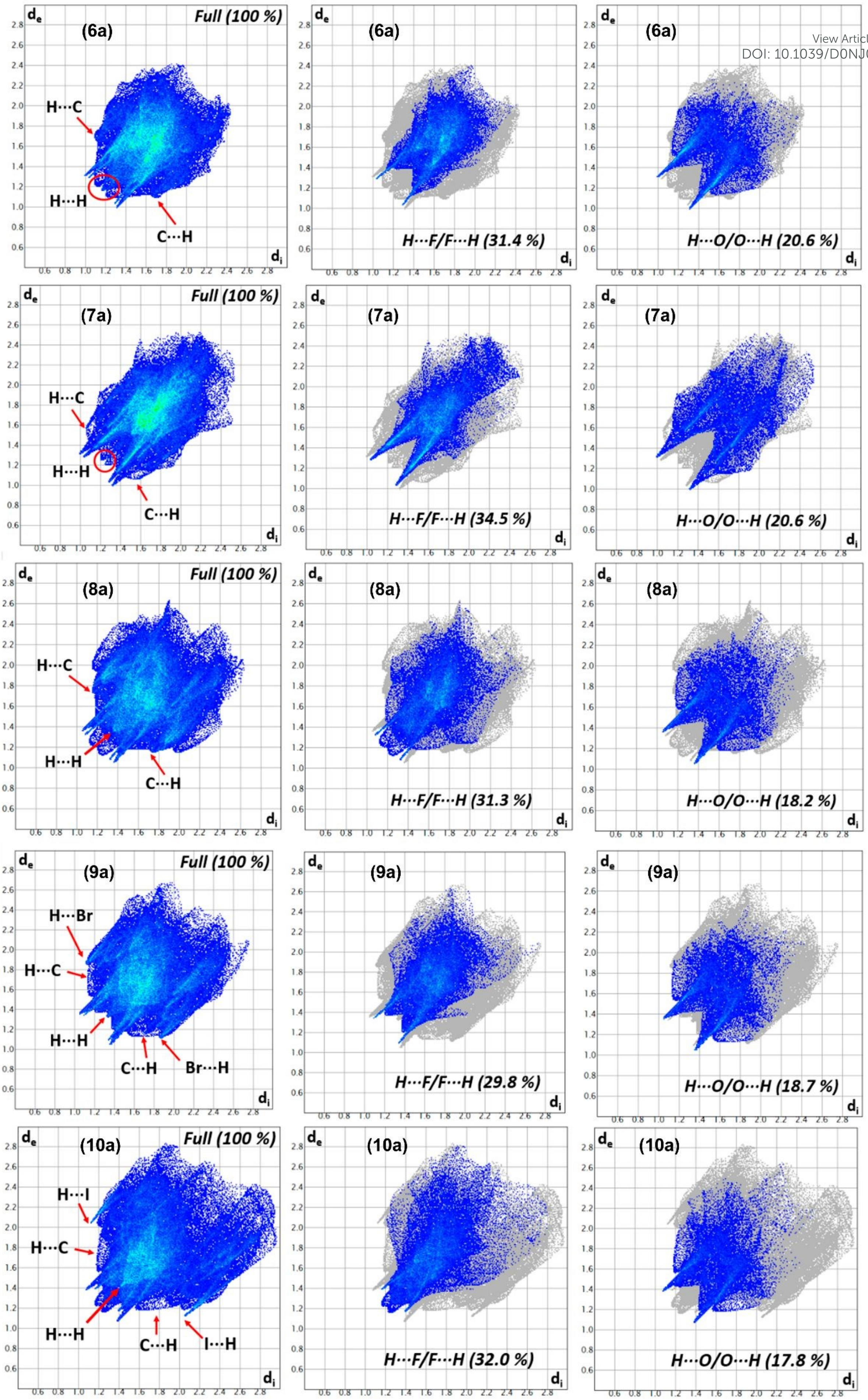

Figure 10. Full and decomposed two dimensional fingerprint plots for pincer-adducts (**6a–10a**) showing the spikes of the main intermolecular interactions.

View Article Online
DOI: 10.1039/D0NJ04328A

3.3. DFT study

As aforementioned, the theoretical study is devoted to analyze and characterize the rare C–F···O interactions by means of QTAIM and NCIplot analysis. First of all, we have computed the MEP surfaces of compounds **6a**, **8a**–**10a** to investigate the charge distribution of the pincer adducts and particularly if it is anisotropic around the F-atoms that participate in the bifurcated F···O_2 interaction. Figure 11 shows the MEP surface of **6a** as a representative model and it can be observed that the most negative region corresponds to the middle of both *O*-bridging atoms (–44.5 kcal/mol). This behavior has been previously analyzed and attributed to through space α-effects.[38] The MEP values at the *O*-atoms of the sulfonamide group are also large and negative. The most positive region corresponds to the H-atoms adjacent to the CF_3 group and in α-position with respect to the bridging *O*-atoms (+23.8 kcal/mol). This MEP distribution strongly agrees with the formation of the self-assembled dimers in the pincer adducts, since the H-bonds involve the most positive and negative regions of the molecule. It is interesting to highlight that the molecular electrostatic potential distribution is anisotropic around the F-atom that participates in the F···O interaction, as highlighted in the left side of Figure 11. By using a reduced MEP scale (± 5 kcal/mol) is can be observed that the MEP is in general small at the F-atom and slightly positive at the region that is closest to the most positive H-atoms (maximum MEP). Therefore, the MEP surface suggests that the F···O contact can be modestly attractive in terms of electrostatics forces.

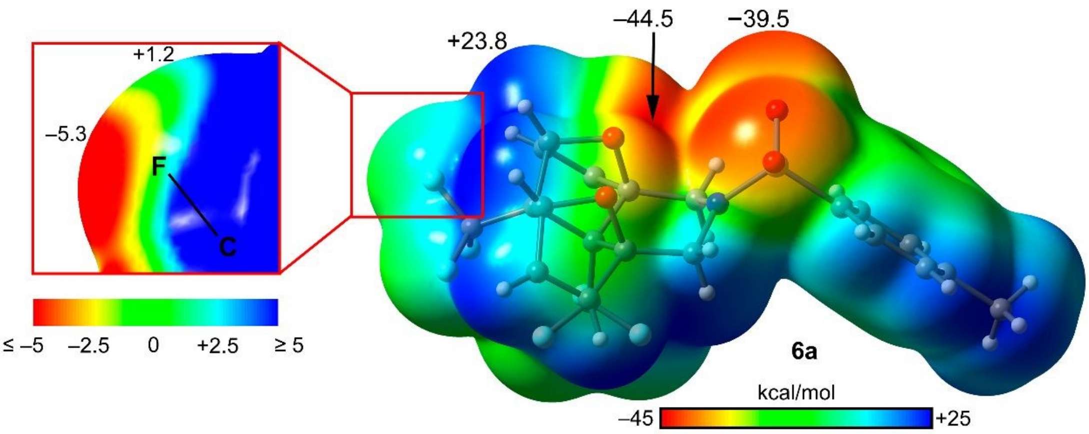

Figure 11. MEP surface (0.001 a.u. envelope) of compound **6a** at the PBE1PBE-D3/def2-TZVP level of theory. The MEP values at selected points are indicated in kcal/mol.

Figure 12 shows the dimers analyzed in this work including the QTAIM distribution of critical points (CPs) and bond paths, the NCIplot surface and the dimerization energies for compounds **6a**,

8a–10a. The dimerization energies are large and similar (ranging to –18.1 to –19.9 kcal/mol) for all compounds in line with the MEP surface shown in Figure 11, since the most positive and negative regions of both molecules interact upon formation of the self-assembled dimers. Interestingly, the QTAIM analysis confirms the existence of the C–H···O bonds depicted in Figure 8 that are characterized by the corresponding bond CPs (red sphere) and bond paths interconnecting the H and O atoms. The NCIplot index surface analysis also shows green isosurfaces (meaning weakly attractive) between the H and O atoms that coincide with the location of the bond CPs. In spite of each individual C–H···O contact is weak (considering the colour of the isosurface), the formation of eight contacts justifies the large dimerization energies. In fact, the green isosurfaces located between the bridging O-atoms and the C–H bonds are large, embracing the whole diepoxybenzo[*de*]isoquinoline moieties of both monomers. The combined QTAIM/NCIplot analysis also evidences the existence of the symmetrically equivalent F···O_2 bifurcated interactions, each one characterized by two bond CPs and bond paths connecting the F-atom to both O-atoms of the sulfonamide group. Figure 12e shows an enlarged representation of the QTAIM/NCIplot analysis where the bond CPs and isosurfaces that characterize the C–H···O and C–F···O contacts can be better appreciated. Both the C–H and C–F bonds are connected to two O-atoms, thus establishing bifurcated interactions. In an effort to evaluate the contribution of the C–F···O interactions, we have also computed the dimerization energies of the CF_3→F mutated dimers (see Figure 12f for a selected example). In this mutated models the CF_3 has been changed by a F-atom with a double purpose. First, to eliminate the bifurcated C–F···O_2 interaction and second, to keep the acidity of the interacting H-atoms similar to that of the original compound, since the electron withdrawing of the CF_3 is similar to that of F. As a result, the dimerization energies are slightly reduced (the differences ΔΔE are summarized in Table 4), thus indicating that the energy associated to the C–F···O contacts is very small (ranging from –0.2 to –0.5 kcal/mol) but favorable. Table 4 also summarizes the values of electron density (ρ), potential energy density (Vr) and total energy density at the bond CPs that characterize the C–F···O interactions. The values of ρ(r) at the bond CPs are small in agreement with the ΔΔE energies. Moreover, the H(r) are positive, thus confirming the noncovalent nature of the interaction.

View Article Online
DOI: 10.1039/D0NJ04328A

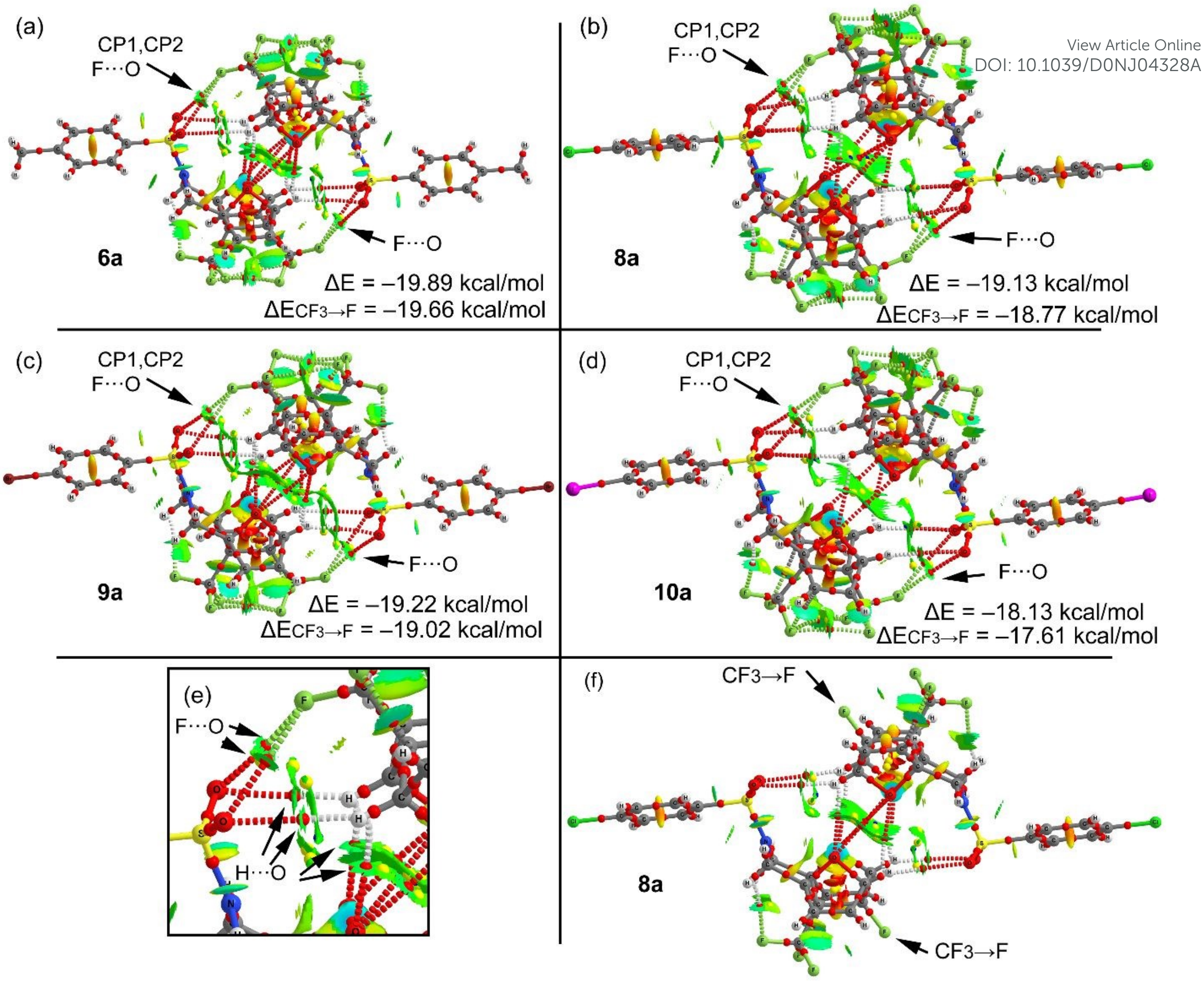

Figure 12. QTAIM distribution of bond, ring and cage CPs (red, yellow and blue spheres respectively) and bond paths for compounds **6a** (a), **8a** (b), **9a** (c), **10a** (d), a closer view of the distribution in **6a** (e) and the mutated model of **8a** (f). The interaction energies of the dimers and CF_3→F mutated dimers are also indicated.

Table 4. QTAIM parameters at the bond CPs that characterize the C–F⋯O interactions (see Figure 12), in atomic units. The ΔΔE energies are given in kcal/mol

Compound	CP#	rho	V(r)	H(r)	ΔΔE
6a	CP1	0.0045	–0.0025	0.0015	0.23
	CP2	0.0047	–0.0027	0.0017	
8a	CP1	0.0045	–0.0025	0.0014	0.34
	CP2	0.0037	–0.0020	0.0013	
9a	CP1	0.0043	–0.0025	0.0015	0.20
	CP2	0.0049	–0.0028	0.0016	
10a	CP1	0.0032	–0.0017	0.0012	0.52
	CP2	0.0039	–0.0019	0.0011	

View Article Online
DOI: 10.1039/D0NJ04328A

Concluding remarks

The synthesis and X-ray structures of a series of hydrogenated 1,4:5,8-diepoxy diepoxynaphthalenes derivatives obtained by tandem [4+2] cycloaddition reactions are reported in this work. An infrequent example of kinetic and thermodynamic reaction control in the course of the reversible intramolecular Diels-Alder reaction of *bis*-furyl dienes with hexafluoro-2-butyne has been discovered. It was found that at ambient temperature pincer-[4+2] cycloadducts are predominately formed, while the exclusive formation of domino-adducts is observed at elevated temperatures. The solid state architecture of the compounds has been described and analyzed by means of Hirshfeld surface analysis and DFT calculations. The solid state assemblies are basically dominated by C–H···O interactions. For the pincer adducts, the formation of self-assembled dimers where unusual $F\cdots O_2$ bifurcated interactions are established has been analyzed in detail by means of tandem QTAIM and NCIplot index surface analyses. They are useful to confirm both the existence and attractive nature of such interaction. The MEP surface calculations indicate that the charge distribution is anisotropic at the F-atom that participates in the F···O interaction. Finally, the energy associated to such contacts has been estimated using mutated dimers and DFT calculations that confirm the attractive nature of the interaction; however, they are extremely weak.

Acknowledgment

Funding for this research was provided by the Russian Science Foundation (RSF) (project number 18-13-00456). We thank the MICIU/AEI from Spain for financial support (project number CTQ2017-85821-R, FEDER funds). We also thank the CTI (UIB) for computational facilities. DMG is Research fellow of CONICET, Argentina.

Conflict of interest

The authors declare no conflict of interest

References

1. S. R. Marsden, L. Mestrom, D. G. G. McMillan, and U. Hanefeld, *ChemCatChem*, 2020, **12**, 426–437.

2. D. L. Boger and S. M. Weinreb, Hetero Diels-Alder Methodology in Organic Synthesis, Vol. 47, Elsevier, Amsterdam, 2012.

3. H. B. Kagan and O. Riant, *Chem. Rev.*, 1992, **92**, 1007–1019.

4. K. C. Nicolaou, S. A. Snyder, T. Montagnon, and G. Vassilikogiannakis, *Angew. Chem. Int. Ed.*, 2002, **41**, 1668–1698.

5. G. Brieger and J. N. Bennett, *Chem. Rev.*, 1980, **80**, 63–97.

6. K. K. Borisova, E. A. Kvyatkovskaya, E. V. Nikitina, R. R. Aysin, R. A. Novikov, and F. I. Zubkov, *J. Org. Chem.,* 2018, **83**, 4840−4850.

7. K. K. Borisova, E. V. Nikitina, R. A. Novikov, V. N. Khrustalev, P. V. Dorovatovskii, Y. V. Zubavichus, M. L. Kuznetsov, V. P. Zaytsev, A. V. Varlamov, and F. I. Zubkov, *Chem. Commun*., 2018, **54**, 2850−2853.

8. G. Cavallo, P. Metrangolo, R. Milani, T. Pilati, A. Priimagi, G. Resnati, and G. Terraneo, *Chem. Rev*., 2016, **116**, 2478–2601.

9. V. R. Hathwar, D. Chopra, P. Panini, and T. N. Guru Row, *Cryst. Growth Des*., 2014, **14**, 5366–5369.

10. (a) D. Dey, S. Bhandary, A. Sirohiwal, V. R. Hathwar, and D. Chopra, *Chem. Commun*., 2016, **52**, 7225−7228; (b) A. Rana, B. Galmes, H. S. Biswal, A. Frontera and D. Chopra Phys. Chem. Chem. Phys. 2020, DOI:10.1039/d0cp05280a

11. P. Panini, R. G. Gonnade, and D. Chopra, *New J. Chem*., 2016, **40**, 4981−5001.

12. V. Elakkat, C.-C. Chang, J.-Y. Chen, Y.-C. Fang, C.-R. Shen, L.-K. Liu, and N. Lu, *Chem. Commun*., 2019, **55**, 14259−14262.

13. L. Krause, R. Herbst-Irmer, G. M. Sheldrick, and D. Stalke, *J. Appl. Cryst.,* 2015, **48**, 3−10.

14. Bruker, *SAINT*, v. 8.29A, Bruker AXS Inc., Madison, WI, 2013.

15. P. R. Evans, *Acta Crystallogr.,* 2006, **D62**, 72−82.

16. T. G. G. Battye, L. Kontogiannis, O. Johnson, H. R. Powell, and A. G. W. Leslie, *Acta Crystallogr.,* 2011, **D67**, 271−281.

17. M. D. Winn, C. C. Ballard, K. D. Cowtan, E. J. Dodson, P. Emsley, P. R. Evans, R. M. Keegan, E. B. Krissinel, A. G. W. Leslie, A. McCoy, S. J. McNicholas, G. N. Murshudov, N. S. Pannu, E. A. Potterton, H. R. Powell, R. J. Read, A. Vagin, and K. S. Wilson, *Acta Crystallogr.,* 2011, **D67**, 235−242.

18. G. M. Sheldrick, *Acta Crystallogr.,* 2015, **A71**, 3−8.

19. G. M. Sheldrick, *Acta Crystallogr.,* 2015, **C71**, 3−8.

20. J. J. McKinnon, M. A. Spackman, and A. S. Mitchell, *Acta Crystallogr*., 2004, **B60**, 627.

21. J. J. McKinnon, D. Jayatilaka, and M. A. Spackman, *Chem. Commun*., 2007, 3814.

22. M. A. Spackman and D. Jayatilaka, *CrystEngComm,* 2009, **11**, 19.

23. M. A. Spackman, *Chem. Rev*., 1992, **92**, 1769.

24. M. J. Turner, J. J. McKinnon, S. K. Wolff, D.J. Grimwood, P. R. Spackman, D. Jayatilaka, and M. A. Spackman, CrystalExplorer17, 2017. University of Western Australia: Perth.

25. Gaussian 16, Revision A.01, M. J. Frisch, G. W. Trucks, H. B. Schlegel, G. E. Scuseria, M. A. Robb, J. R. Cheeseman, G. Scalmani, V. Barone, G. A. Petersson, H. Nakatsuji, X. Li, M. Caricato,

A. V. Marenich, J. Bloino, B. G. Janesko, R. Gomperts, B. Mennucci, H. P. Hratchian, J. V. Ortiz, A. F. Izmaylov, J. L. Sonnenberg, D. Williams-Young, F. Ding, F. Lipparini, F. Egidi, J. Goings, B. Peng, A. Petrone, T. Henderson, D. Ranasinghe, V. G. Zakrzewski, J. Gao, N. Rega, G. Zheng, W. Liang, M. Hada, M. Ehara, K. Toyota, R. Fukuda, J. Hasegawa, M. Ishida, T. Nakajima, Y. Honda, O. Kitao, H. Nakai, T. Vreven, K. Throssell, J. A. Montgomery, Jr., J. E. Peralta, F. Ogliaro, M. J. Bearpark, J. J. Heyd, E. N. Brothers, K. N. Kudin, V. N. Staroverov, T. A. Keith, R. Kobayashi, J. Normand, K. Raghavachari, A. P. Rendell, J. C. Burant, S. S. Iyengar, J. Tomasi, M. Cossi, J. M. Millam, M. Klene, C. Adamo, R. Cammi, J. W. Ochterski, R. L. Martin, K. Morokuma, O. Farkas, J. B. Foresman, and D. J. Fox, Gaussian, Inc., Wallingford CT, 2016

26. S. F. Boys and F. Bernardi, *Mol. Phys.,* 1970, **19**, 553−566.

27. D. Rappoport and F. Furche, *J. Chem. Phys.,* 2010, **133**, 134105.

28. F. Weigend and R. Ahlrichs, *Phys. Chem. Chem. Phys.,* 2005, **7**, 3297−3305.

29. J. P. Perdew, K. Burke, and M. Ernzerhof, *Phys. Rev. Lett.,* 1996, **77**, 3865−3868.

30. J. P. Perdew, M. Ernzerhof, and K. Burke, *J. Chem. Phys.,* 1996, **105**, 9982−9985.

31. (a) S. Grimme, *J. Comput. Chem.,* 2006, **27**, 1787−1799; (b) S. Grimme, J. Antony, S. Ehrlich, and H. Krieg, *J. Chem. Phys.,* 2010, **132**, 154104.

32. (a) E. R. Johnson, S. Keinan, P. Mori-Sánchez, J. Contreras-García, A. J. Cohen, and W. Yang, *J. Am. Chem. Soc.,* 2010, **132**, 6498−6506; (b) J. Contreras-García, E. R. Johnson, S. Keinan, R. Chaudret, J.-P. Piquemal, D. N. Beratan, and W. Yang, *J. Chem. Theory Comput.,* 2011, **7**, 625−632.

33. AIMAll (Version 19.10.12), Todd A. Keith, TK Gristmill Software, Overland Park KS, USA, 2019 (aim.tkgristmill.com).

34. (a) L. A. Barrios, G. Aromi, A. Frontera, D. Quinonero, P. M Deya, P. Gamez, O. Roubeau, E. J. Shotton, S. J. Teat, *Inorg. Chem*., 2008, **47**, 5873-5881; (b) M. Mirzaei, H. Eshtiagh-Hosseini, Z. Bolouri, Z. Rahmati, A. Esmaeilzadeh, A. Bauza, P. Ballester, M. Barcelo-Oliver, J. T Mague, B. Notash and A. Frontera, *Cryst. Growth Des*., 2015, **15**, 1351-1361; (c) P. Manna, S. K. Seth, M. Mitra, S. R. Choudhury, A. Bauzá, A. Frontera and S. Mukhopadhyay, *Cryst. Growth Des*., 2014, **14**, 5812-5821.

35. (a) L. E. Zelenkov, D. M. Ivanov, K. Sadykov, N. A. Bokach, B. Galmes, A. Frontera and V. Yu. Kukushkin, Vadim Yu. *Cryst. Growth Des*., 2020, **20**, 6956-6965; (b) N. S. Soldatova, P. S. Postnikov, V. V. Suslonov, T. Yu. Kissler, D. M. Ivanov, M. S. Yusubov, B. Galmes, A. Frontera and V. Yu. Kukushkin, *Org. Chem. Front*. 2020, **7**, 2230-2242; (c) E. A. Katlenok, M. Haukka, O. V. Levin, A. Frontera, V. Yu. Kukushkin, *Chem. Eur. J.* 2020, **26**, 7692-7701; (d) A. V. Rozhkov, A. A: Eliseeva, S. V. Baykov, B. Galmes, A. Frontera and V. Yu. Kukushkin, *Cryst.*

Growth Des. 2020, **20**, 5908-5921; (e) A. V. Rozhkov, I. V. Ananyev, R. M. Gomila, A. Frontera and V. Yu. Kukushkin, *Inorg. Chem*. 2020, **59**, 9308-9314.

View Article Online
DOI: 10.1039/D0NJ04328A

36. (a) A. Singh, D. K. Sahoo, S: K. Sethi, S. Jena and H. S. Biswal, *ChemPhysChem*, 2017, **18**, 3625-3633; (b) D. J. Wolstenholme, T. T. Titah, F. N. Che, K. T. Traboulsee, J. Flogeras and G. S. McGrady, *J. Am. Chem. Soc.*, 2011, **133**, 16598-16604; (c) C. F. Matta, J. Hernández-Trujillo, T. H. Tang and R. F. W. Bader, *Chem. Eur. J.*, 2003, **9**, 1940– 1951; (d) J. Poater, M. Solà and F. M. Bickelhaupt, *Chem. Eur. J.*, 2006, **12**, 2889– 2895; (e) J. Hernández-Trujillo, C. F. Matta, *Struct. Chem*. 2007, **18**, 849– 857; (f) S. Grimme, C. Mück-Lichtenfeld, G. Erker, G. Kehr, H. Wang, H. Beckers and H. Willner, *Angew. Chem. Int. Ed.*, 2009, **48**, 2592– 2595; (g) F. Weinhold, P. R. Schleyer and W. C. McKee, *J. Comput. Chem.*, 2014, **35**, 1499– 1508

37. D. A. Safin, M. G. Babashkina, K. Robeyns, M. P. Mitoraj, P. Kubisiak and Y. Garcia, *Chem. Eur. J.*, 2015, **21**, 16679-16687.

36. E. A. Kvyatkovskaya, E. V. Nikitina, V. N. Khrustalev, B. Galmés, F. I. Zubkov, and A. Frontera, *Eur. J. Org. Chem.*, 2020, 156−161.

View Article Online
DOI: 10.1039/D0NJ04328A

This manuscript reports the synthesis, X-ray characterization and theoretical study of 3a,6:7,9a-diepoxybenzo[*de*]isoquinoline derivatives focusing on the importance of F···O interactions